



Bridged Semantic Alignment for Zero-shot 3D Medical Image Diagnosis

Haoran Lai^{a,b}, Zihang Jiang^{a,b,*}, Qingsong Yao^c, Rongsheng Wang^{a,b}, Zhiyang He^d, Xiaodong Tao^d, Wei Wei^e, Weifu Lv^f, S. Kevin Zhou^{a,g,h,i,*}

^aSchool of Biomedical Engineering, Division of Life Sciences and Medicine, University of Science and Technology of China, Hefei, Anhui, 230026, P.R.China

^bSuzhou Institute for Advanced Research, University of Science and Technology of China, Suzhou, Jiangsu, 215123, P.R.China

^cStanford University, Palo Alto, California, 94305, United State

^dMedical Business Department, iFlytek Co.Ltd, Hefei, Anhui, 230088, China

^eThe First Affiliated Hospital of USTC, Division of Life Sciences and Medicine, University of Science and Technology of China, Hefei, Anhui, 230001, China

^fDepartment of Radiology, The First Affiliated Hospital of USTC, Division of Life Sciences and Medicine, University of Science and Technology of China, Hefei, 230001, Anhui, China.

^gCenter for Medical Imaging, Robotics, Analytic Computing & Learning (MIRACLE), Suzhou Institute for Advance Research, USTC, Suzhou Jiangsu, 215123, China

^hState Key Laboratory of Precision and Intelligent Chemistry, University of Science and Technology of China, Hefei, Anhui 230026, China

ⁱKey Lab of Intelligent Information Processing of Chinese Academy of Sciences (CAS), Institute of Computing Technology, CAS, Beijing 100190, China

ARTICLE INFO

Article history:

Received xxx

Received in final form xxx

Accepted xxx

Available online xxx

Communicated by xxx

Keywords: Computed tomograph, Vision-language alignment, Zero-shot learning, Cross-modal interaction

ABSTRACT

3D medical images such as Computed tomography (CT) are widely used in clinical practice, offering a great potential for automatic diagnosis. Supervised learning-based approaches have achieved significant progress but rely heavily on extensive manual annotations, limited by the availability of training data and the diversity of abnormality types. Vision-language alignment (VLA) offers a promising alternative by enabling zero-shot learning without additional annotations. However, we empirically discover that the visual and textural embeddings after alignment endeavors from existing VLA methods form two well-separated clusters, presenting a wide gap to be bridged. To bridge this gap, we propose a Bridged Semantic Alignment (BrgSA) framework. First, we utilize a large language model to perform semantic summarization of reports, extracting high-level semantic information. Second, we design a Cross-Modal Knowledge Interaction (CMKI) module that leverages a cross-modal knowledge bank as a semantic bridge, facilitating interaction between the two modalities, narrowing the gap, and improving their alignment. To comprehensively evaluate our method, we construct a benchmark dataset that includes 15 underrepresented abnormalities as well as utilize two existing benchmark datasets. Experimental results demonstrate that BrgSA achieves state-of-the-art performances on both public benchmark datasets and our custom-labeled dataset, with significant improvements in zero-shot diagnosis of underrepresented abnormalities.

© 2025 Elsevier B. V. All rights reserved.

1. Introduction

Computed Tomography (CT) is a widely utilized non-invasive diagnostic tool in clinical practice, playing a crucial role in detecting various abnormalities (Ginat and Gupta, 2014;

*Corresponding author

e-mail: skevinzhou@ustc.edu.cn (S. Kevin Zhou)

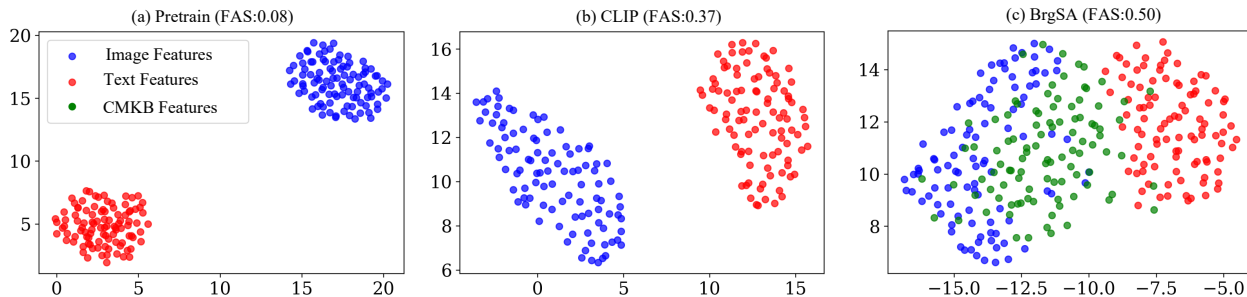


Fig. 1. UMAP visualization of features. Cosine similarity is used to evaluate the alignment between image and text features. The text features are generated using generic descriptive texts to ensure that all images can be matched to all texts. (a) Features generated using pretrained weights without vision-language alignment, where image (in blue) and text features (in red) remain unaligned. (b) Features after vision-language alignment using 3D CLIP, showing improved alignment but with noticeable modality gaps. (c) Features after vision-language alignment using BrgSA framework, where the CMKB features (in green) serve as a bridge to reduce the modality gap and further enhance feature alignment.

Oikonomou et al., 2018; Bera et al., 2019). With the rapid development of artificial intelligence, significant progress has been made in leveraging CT images for automated abnormality diagnosis (Svoboda, 2020). Supervised learning methods have achieved impressive performance in tasks such as disease classification and detection (He et al., 2021; Wang et al., 2022b; Zhang et al., 2022; Li et al., 2023b; Zhang et al., 2024a; Qian et al., 2024; Wang et al., 2024; Mei et al., 2025). However, supervised learning methods heavily rely on large-scale, manually annotated datasets, which is both time-consuming and labor-intensive (Huang et al., 2023; Geuenich et al., 2024). Moreover, the reliance on extensive annotations limits the diversity of available training data, particularly for rare diseases, where labeled samples are exceedingly scarce (Taherdoost, 2024). This constraint hampers the scalability of supervised learning methods and diminishes their ability to generalize across a wide spectrum of diseases (Yoon et al., 2023).

Recently, zero-shot learning (ZSL) based on vision-language alignment has emerged as a promising alternative to traditional supervised learning methods (Long et al., 2017; Zhang et al., 2024b). By eliminating the need for extensive manual annotations, ZSL offers a more efficient path to diagnose a diverse range of abnormalities. For instance, CLIP (Radford et al., 2021) leverages contrastive learning on large-scale image-text datasets to enable effective vision-language alignment and perform zero-shot classification without extensive manual annotations (Zhao et al., 2023). In the medical domain, several studies have demonstrated the potential of CLIP for zero-shot abnormality diagnosis on 3D CT volumes (Hamamci et al., 2024; Cao et al., 2024; Blankemeier et al., 2024; Anonymous, 2024). However, our experiments reveal that directly applying CLIP to 3D medical images remains inadequate in vision-language alignment, as the embedding space exhibits a **significant modality gap**. Specifically, Fig. 1(a) shows the feature space when only pretrained weights are used without introducing vision-language alignment; a clear gap appears between the two clusters of image and text features. The feature alignment score (FAS), which is a metric that quantifies the degree of vision-language alignment and is mathematically defined later in Section 5, is only 0.08. Note that the FAS ranges from 0 to 1, where 0 indicates no alignment between features and 1 signifies

complete alignment. Fig. 1(b) represents the feature space after applying CLIP for 3D vision-language alignment. It is evident that, after alignment, the gap between image and text features appears more narrow than before alignment (FAS is improved to 0.37 from 0.08) but remains pronounced, fundamentally limiting the model’s ability to fully exploit zero-shot abnormality diagnosis on 3D CT volumes. These findings are consistent with previous studies in the natural domain that have identified a pronounced modality gap within the CLIP embedding space, hindering alignment performance (Liang et al., 2022; Tyschchuk et al., 2023; Schrodri et al., 2024; Eslami and de Melo, 2024). This highlights the necessity of addressing the modality gap in CLIP embeddings to achieve better alignment in 3D medical images.

In this paper, we propose a **Bridged Semantic Alignment (BrgSA)** framework, which aims to bridge the modality gap and facilitate effective vision-language alignment. Our approach consists of two modules: semantic summarization and cross-modal knowledge interaction (CMKI). First, we utilize a large language model (LLM), which has powerful semantic understanding capabilities, to summarize clinical reports and extract critical information. This significantly reduces the learning difficulty on the textual side and produces high-level semantic features. Next, we propose a CMKI module to supplement the conventional CLIP alignment, where a cross-modal knowledge bank (CMKB) acts as a semantic bridge between image and text features. By projecting image and text features into the shared latent space of the CMKB, it reduces the discrepancy between modalities and simultaneously preserves their unique characteristics. This enables an implicit alignment approach that does not rely on paired image-text data. Finally, we employ contrastive learning to compare positive and negative pairs, achieving explicit vision-language alignment. Fig. 1(c) visualizes CMKB serving as a bridge between image and text features, effectively narrowing the modality gap. Also, the FAS is further improved to 0.50, indicating a better alignment.

To explore the potential of our vision-language alignment approach for zero-shot diagnosis, we expand the original 18 abnormality labels on CT-RATE (Hamamci et al., 2024) with 15 additional labels. The new benchmark, referred to as “CT-RATE-LT,” focuses on underrepresented abnormalities with

limited occurrences in the dataset, providing a challenging yet valuable testing ground for evaluating diagnostic methods. Experimental results on CT-RATE-LT demonstrate that our method achieves excellent performance in diagnosing under-represented abnormalities, showing significant improvements compared to the existing state-of-the-art (SOTA) method (AUC: 76.9 vs. 85.6). Furthermore, we evaluate our method on the benchmark CT-RATE and RAD-ChestCT (Draeos *et al.*, 2021) datasets, achieving SOTA performances in zero-shot abnormality diagnosis, with an AUC of 79.2 and 70.0 on internal and external validation, respectively. In addition to its diagnostic capabilities, our method significantly outperforms the SOTA in the report-to-volume retrieval task (Recall@10: 5.0 vs. 10.1), demonstrating effective semantic alignment between image and text features.

The main contributions of this work are as follows:

- We propose a BrgSA framework, consisting of semantic report summarization and cross-modal knowledge interaction, which effectively acts as a bridge between the visual and texture features embeddings and hence forges a better vision-and-language alignment.
- We introduce an expanded benchmark dataset, named “CT-RATE-LT”, for 3D medical image analysis, encompassing 15 underrepresented abnormalities, which provides an effective tool for evaluating the zero-shot diagnosis capabilities on long-tailed minor diseases.
- Our method achieves SOTA performance on zero-shot tasks across both internal and external validation datasets, demonstrating its effectiveness in diagnosing various abnormalities and its strong capability in the report-to-volume retrieval task.

2. Related Work

2.1. Medical Vision-language Pretraining

Existing medical vision-language pretraining (VLP) research is predominantly focused on 2D imaging. Open-source datasets like MIMIC-CXR (Johnson *et al.*, 2019) have provided a solid foundation for the advancement of 2D VLP, while PadChest (Bustos *et al.*, 2020), which encompasses 193 abnormality categories, has established an effective benchmark for rare disease diagnosis. GLoRIA (Huang *et al.*, 2021a) enhances the ability to capture associations between images and text by integrating global and local feature alignment. CheXZero (Tiu *et al.*, 2022) leverages a CLIP model pre-trained on natural data, achieving stable improvements in medical VLP performance. MedCLIP (Wang *et al.*, 2022c) employs unpaired medical images and text with a semantic matching loss to mitigate false negatives. Xplainer (Pellegrini *et al.*, 2023) introduces an explainable zero-shot diagnosis framework based on observation-driven contrastive learning. MedKLIP (Wu *et al.*, 2023) and KAD (Zhang *et al.*, 2023b) incorporate domain-specific medical knowledge to improve VLP performance in CXR diagnosis tasks. CARZero (Lai *et al.*, 2024) advances cross-modal alignment by leveraging cross-attention mechanisms to address

the complex relationships between visual and textual modalities. These advancements have established 2D VLP as a robust framework for various abnormalities diagnosis.

Recently, many researches have begun extending VLP to 3D medical images. CT-CLIP (Hamamci *et al.*, 2024) combines spatial and causal transformers in 3D vision encoder. BIUD (Cao *et al.*, 2024) enhances 3D CT performance by distilling knowledge from CXR models. CT-GLIP (Lin *et al.*, 2024) and fVLM (Anonymous, 2024) propose anatomical structure alignment strategies to achieve organ-level feature alignment. Merlin (Blankemeier *et al.*, 2024) introduces a two-step process, first optimizing the visual encoder with supervised labels and then training for vision-language alignment. Despite these advances, previous methods have overlooked the significant modality gap in CLIP embedding spacing for 3D medical imaging-report alignment, limiting the performance of zero-shot abnormality diagnosis.

2.2. Multi-Modality Interaction

Cross-modal interaction has been extensively explored to bridge the gaps between different modalities, such as vision and language modalities. Transformer-based approaches like ViL-BERT (Lu *et al.*, 2019) employs dual-stream transformers with co-attentional layers for modality-specific processing, while ViLT (Kim *et al.*, 2021) uses a unified transformer to jointly encode visual patches and textual embeddings, enabling more efficient cross-modal interaction. MGCA (Wang *et al.*, 2022a) introduces cross-attention mechanisms to achieve cross-modal interaction, aligning medical image and text representations at multiple levels. MPMA (Zhang *et al.*, 2023a) enhances cross-modal interaction by integrating image-text reconstruction with a global and local alignment mechanism, enabling richer semantic representation learning. However, these approaches primarily emphasize explicit alignment mechanisms, often overlooking the potential of leveraging shared semantic spaces to guide cross-modal learning effectively.

Dictionary learning has emerged as a powerful technique for enhancing cross-modal alignment by constructing shared representational spaces. Deng *et al.* (2015) aligns features via a shared label space to improve cross-modal retrieval. HCDDL (Li *et al.*, 2023a) builds hierarchical semantic embeddings by dictionary learning for fine-grained alignment. UNIMO-2 (Li *et al.*, 2022) leverages grounded semantic spaces to bridge visual and textual modalities, effectively addressing misalignment issues. Methods such as DetCLIP (Yao *et al.*, 2022) and SOHO (Huang *et al.*, 2021b) further exploit trainable dictionaries to enrich visual-semantic representations, achieving SOTA results in zero-shot and vision-language tasks. CP-CLIP (Yu *et al.*, 2024) employs the Core-Periphery principle to facilitate cross-modal interaction by structuring shared semantics and modality-specific features within a unified latent space. Despite these advancements, existing methods often fail to fully exploit the potential of shared representational spaces in improving vision-language alignment. To address this limitation, we propose a cross-modal knowledge interaction module that leverages shared representational spaces to achieve semantic-guided image learning without risking cross-modal information leakage.

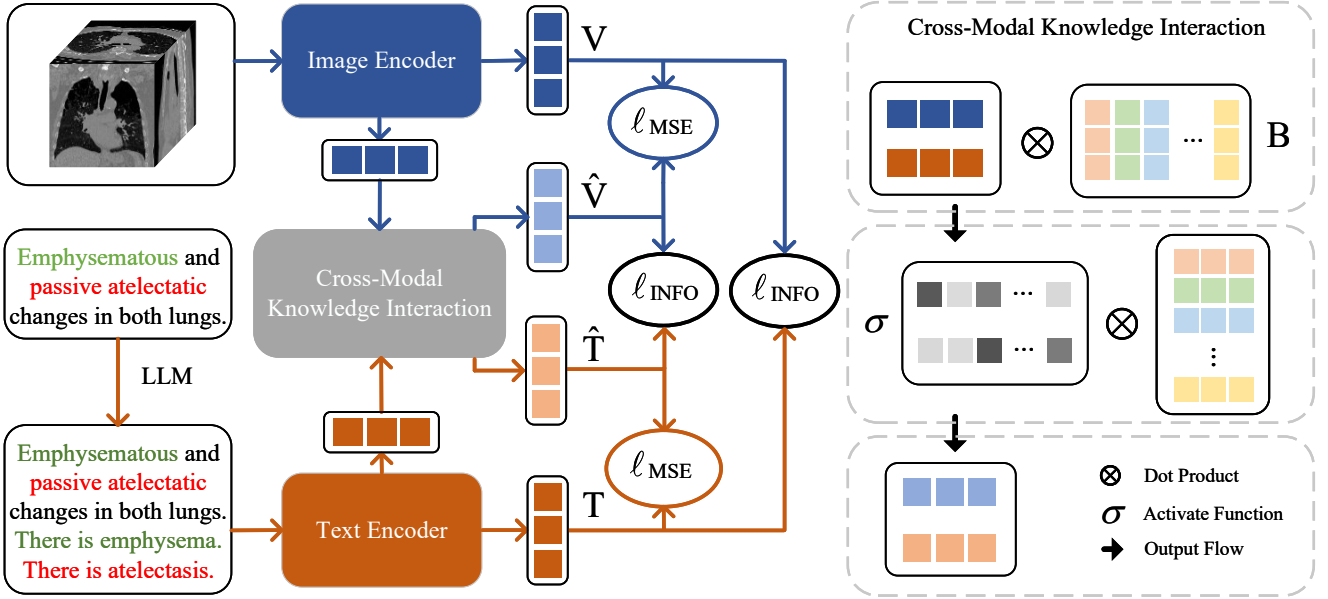


Fig. 2. Illustration of the proposed BrgSA network, which integrates semantic summarization and cross-modal knowledge interaction (CMKI). First, we leverage a large language model (LLM) to summarize the report, generating outputs in a fixed template. These summarized reports, along with the original reports, serve as the textual inputs. Then, image and text features are extracted by respective encoders and fed into CMKI module to obtain interaction features. Finally, the interaction features are constrained using an MSE loss, while alignment optimization is achieved via an InfoNCE loss.

3. Method

In this section, we describe our proposed BrgSA framework for zero-shot classification. As illustrated in Fig. 2, BrgSA consist of semantic summarization and CMKI module. More details are introduced in the following.

3.1. Semantic Summarization

To simplify learning on the textual side, we introduce semantic summarization. In the context of medical reports, textual data often contains lengthy and complex descriptions, including both critical abnormality-related information and a significant amount of irrelevant details. Such data characteristics increase the difficulty of extracting and aligning core semantic information with image features. We leverage the powerful semantic understanding and summarization capabilities of LLM to produce semantic summaries of medical reports, which are much easier to understand. As illustrated in Fig. 3, a prompt is designed to guide the LLM in extracting key abnormality-related information and generating outputs in a fixed template: “There is [abnormality].” Compared to directly processing the original text, this template-based summarization significantly reduces the difficulty of learning on the textual side. Furthermore, by combining the original reports with the LLM-generated summaries as input, the semantic richness of the textual data is preserved.

3.2. Feature Extraction

Assume that the training dataset contains N samples denoted as $S_{\text{train}} = \{(I_1, R_1), \dots, (I_N, R_N)\}$, where $I_i \in \mathbb{R}^{H \times W \times D}$ represents a 3D CT volume and R_i represents its corresponding medical report. Here, H, W, D denote the height, width, and depth of the 3D CT volumes, respectively. As illustrated in Fig. 2, we

Prompting LLM to generate semantic summarization

prompts = [You now assume the role of a knowledgeable radiologist. Please assist me in summarizing medical reports, extracting disease information and generating this information using a fixed template. The template format includes: "There is [D]", where [D] represents the describing information of diseases obtained from the report. Please generate sentences according to the given format one by one.
 Given an Example:
 "Report": As far as can be seen; A stable soft tissue mass of approximately 5x4x5. On the right, both thyroid glands have increased in size and their parenchyma is heterogeneous. US control is recommended. Trachea and lumen of both main bronchi are open.
 "system": There is hiatal hernia. There is lung nodule. There is pulmonary fibrotic sequela. There is peribronchial thickening."
 Example END.,
 "Report": {report}]

Fig. 3. Prompt for LLM used in semantic summarization for reports.

introduce the components of our architecture for feature extraction, including an image encoder Φ_I for CT images and a text encoder Φ_R for medical reports.

Image Encoder The image encoder is designed to extract global features from 3D CT images, as shown in Eq. 1.

$$V_i = \Phi_I(I_i), \quad (1)$$

where $V_i \in \mathbb{R}^d$ represents the global features of the image, and d denotes the feature dimension. In our experiments, we adopt a ViT-base (Dosovitskiy et al., 2020) model as the image encoder. The [CLS] token is used to represent the global feature for 3D image.

Text Encoder The text encoder is used to extract global fea-

tures from the medical report, as shown in Eq. 2.

$$T_i = \Phi_R(R_i), \quad (2)$$

where $T_i \in \mathbb{R}^d$ represents the global features of the medical report. We use PubMedBERT (Gu *et al.*, 2021) as the text encoder, which is well-suited for medical-related tasks due to its pretraining on biomedical literature. We use global average pooling for all non-[PAD] tokens as the global features of the text. In our experiment, the output feature dimensions of both the image and text encoders are unified to d .

3.2.1. Cross-Modal Knowledge Interaction

To bridge the gap between 3D medical images and textual reports and enhance vision-language alignment, we propose the CMKI module, as shown in Fig. 2. This module effectively reduces cross-modal discrepancies, improves inter-modal similarity, and preserves the unique characteristics of each modality, thereby enhancing the overall quality of vision-language alignment.

In the CMKI module, we introduce a CMKB as a bridge for image-text interaction. The CMKB is initialized as a set of learnable embeddings:

$$\mathbf{B} = \{\mathbf{b}_1, \mathbf{b}_2, \dots, \mathbf{b}_K\}, \quad \mathbf{b}_k \in \mathbb{R}^d, \quad (3)$$

where K represents the number of basis vectors.

To construct a bridge between the image and text features, we first calculate the similarity between the image features V_i and the CMKB basis vectors \mathbf{B} . This similarity is calculated using the inner product:

$$\text{sim}(\mathbf{B}, V_i) = \mathbf{B}^T V_i, \quad (4)$$

where $\text{sim}(\mathbf{B}, V_i)$ represents the similarity between the image feature V_i and each basis vector in the CMKB. The similarity scores are then normalized using a softmax function to produce attention weights:

$$\mathbf{Z}_i^V = \text{softmax}(\text{sim}(\mathbf{B}, V_i)). \quad (5)$$

Here, \mathbf{Z}_i^V denotes the attention weights that highlight the contribution of each basis vector to the reconstruction of V_i . Similarly, for the text features T_i , the attention weights \mathbf{Z}_i^T is calculated as:

$$\mathbf{Z}_i^T = \text{softmax}(\text{sim}(\mathbf{B}, T_i)). \quad (6)$$

These attention weights are used to identify the most relevant basis vectors from the CMKB for representing the image and text features.

Using the attention weights \mathbf{Z}_i^V and \mathbf{Z}_i^T , the original image and text features are reconstructed by taking a weighted sum of the CMKB basis vectors:

$$\hat{V}_i = \mathbf{B} \cdot \mathbf{Z}_i^V, \quad \hat{T}_i = \mathbf{B} \cdot \mathbf{Z}_i^T. \quad (7)$$

In this process, the CMKB captures the common features shared by the image and text modalities, enabling cross-modal information exchange.

We use a reconstruction loss to optimize the CMKB. The loss function is defined as:

$$\ell_{\text{MSE}} = \frac{1}{N} \sum_{i=1}^N (\|V_i - \hat{V}_i\|_2^2 + \|T_i - \hat{T}_i\|_2^2). \quad (8)$$

The reconstruction mechanism ensures that the CMKB functions as an effective bridge for image-text interaction by capturing critical information from both modalities, facilitating cross-modal knowledge exchange, and reducing modality discrepancies. By narrowing the modality gap, the CMKI module enhances the alignment between 3D CT volumes and textual reports, thereby improving the effectiveness of CLIP's training. Specifically, our method minimizes cross-modal discrepancies, allowing CLIP to more effectively reduce the distance between paired image-text features and increase the distance between unpaired ones during contrastive learning. Furthermore, the use of CMKB as an intermediary maintains the independence of image and text features, preventing information leakage between positive and negative pairs in contrastive learning. This design ensures robust and unbiased feature learning while enhancing vision-language alignment.

To ensure vision-language alignment, we employ a symmetric InfoNCE loss between image and text features:

$$\ell_{\text{INFO}} = -\frac{1}{N} \sum_{i=1}^N \log \frac{\exp(\text{sim}(V_i, T_i)/\tau)}{\sum_j \exp(\text{sim}(V_i, T_j)/\tau)}, \quad (9)$$

where $\text{sim}(\cdot, \cdot)$ denotes cosine similarity, and τ is a temperature parameter. Additionally, we apply the same InfoNCE loss to the reconstructed features:

$$\ell_{\text{INFO-R}} = -\frac{1}{N} \sum_{i=1}^N \log \frac{\exp(\text{sim}(\hat{V}_i, \hat{T}_i)/\tau)}{\sum_j \exp(\text{sim}(\hat{V}_i, \hat{T}_j)/\tau)}. \quad (10)$$

The total alignment loss combines the reconstruction and InfoNCE losses:

$$\ell_{\text{total}} = \alpha \ell_{\text{MSE}} + \beta \ell_{\text{INFO}} + \gamma \ell_{\text{INFO-R}}, \quad (11)$$

where α , β , and γ are hyperparameters controlling the contributions of the reconstruction loss (ℓ_{MSE}), the InfoNCE loss (ℓ_{INFO}), and the InfoNCE loss on reconstructed features ($\ell_{\text{INFO-R}}$), respectively.

4. Experiments

4.1. Materials

We conduct experiments on two publicly available datasets: CT-RATE and RAD-ChestCT. The CT-RATE dataset consists of 3D CT volumes paired with medical reports, providing a valuable resource for evaluating cross-modal alignment methods in the medical domain. The RAD-ChestCT dataset includes 3D CT volumes with detailed annotations of various abnormalities, enabling the assessment of zero-shot diagnosis performance. Detailed descriptions of the datasets are as follows:

CT-RATE The CT-RATE dataset comprises 25,692 non-contrast chest CT volumes, expanded to 50,188 volumes

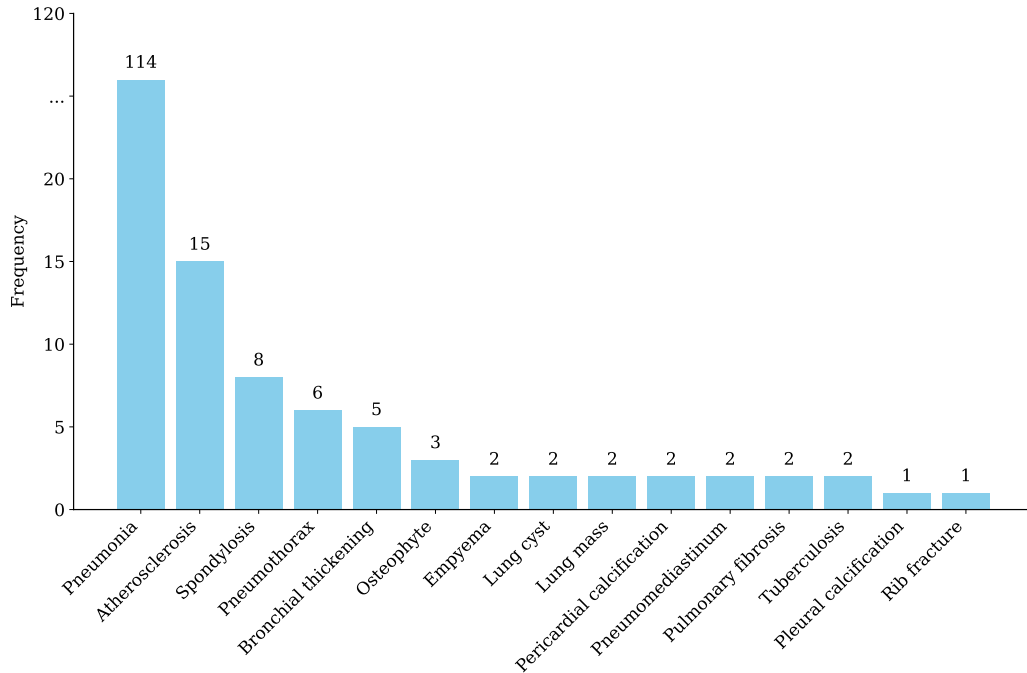


Fig. 4. Histogram of abnormality frequencies for CT-RATE-LT.

through various reconstruction techniques, originating from 21,304 unique patients. Each CT volume is paired with a corresponding radiology report. A total of 47,149 CT volumes with corresponding reports are used for training, while 3,039 CT volumes are reserved for internal validation. The dataset includes 18 abnormality labels, extracted from reports using an automated algorithm. To further evaluate the zero-shot detection capabilities of our method, we curate 15 underrepresented abnormality labels from the validation set by GPT-4 (Achiam *et al.*, 2023)¹, reflecting a long-tail distribution, to construct an extended **CT-RATE-LT** dataset. All curated labels are manually corrected by a radiologist to ensure annotation accuracy. The frequency of abnormalities in CT-RATE-LT is shown in Fig. 4.

RAD-ChestCT The RAD-ChestCT dataset contains 3,630 CT volumes, uniformly reconstructed using a single technique. This dataset includes 84 abnormality labels. As part of our external validation, as shown in Fig. 5, 27 abnormalities from RAD-ChestCT are mapped to the 18 abnormalities in CT-RATE to ensure consistency. To further demonstrate the strength of our method, we refer to the remaining 56 abnormalities from RAD-ChestCT as **RAD-ChestCT-LT** and evaluate the zero-shot diagnosis performance on these additional abnormalities. Note that the abnormality, “other_path”, is excluded from our analysis due to its lack of meaningful semantic descriptions.

4.2. Dataset Preprocessing

For the image data, we unify the spacing of CT volumes to (1.5 mm, 1.5 mm, 3 mm), to ensure uniform resolution across

the datasets. Random cropping is employed during the training stage to generate input volumes with a shape of (224, 224, 112), which balances computational efficiency and sufficient spatial coverage for 3D images. The patch size in the ViT-base model is set to (16, 16, 8), following the adaptation for 3D inputs. To enhance feature representation, CT images are clipped to a Hounsfield Unit (HU) range of [−1000, 1000], which focuses on clinically relevant tissues, and normalized to the pixel intensity range [−1, 1].

For the text data, we process both the original reports and the semantic summaries generated by GPT-4, splitting them into shorter sentences for analysis. As part of our data augmentation strategy, five sentences are randomly sampled and concatenated into a longer sentence during training, enabling diverse text representations that better capture the variability in medical reporting styles. This augmented sentence serves as the corresponding image report, improving the robustness of vision-language alignment.

4.3. Implementation Details

In our experiments, we adapt ViT-B/16 as the image encoder by replacing the 2D convolutional layers in patch embedding module with 3D convolutional layers, resulting in a 3D ViT-B/16 architecture. For the text encoder, we fine-tune PubMedBERT on the text data of the CT-RATE dataset to better capture the linguistic characteristics and representation requirements of the medical domain. Furthermore, we utilize M3AE (Chen *et al.*, 2022) for pretraining the image and text encoders. M3AE employs a masked cross-modal reconstruction strategy, where masked regions in one modality are reconstructed using information from the other modality. This approach enhances

¹<https://openai.com/index/gpt-4/>

Table 1. Zero-shot abnormality diagnosis performance comparison across internal (CT-RATE) and external (RAD-ChestCT) validation benchmarks, including shape dimensions $[H, W, D]$ and voxel spacing (mm). The best performance is highlighted as bold.

| Method | Setting | Shape $[H, W, D]$ | Spacing (mm) | CT-RATE | | | | RAD-ChestCT | | | |
|-----------|-------------|----------------------|-------------------|-------------|-------------|-------------|-------------|-------------|-------------|-------------|-------------|
| | | | | AUC | ACC | F1 score | Precision | AUC | ACC | F1 score | Precision |
| CT-Net | Supervised | [420, 420, 402] | – | 60.3 | 58.1 | 63.1 | 23.9 | 54.4 | 54.0 | 58.7 | 28.5 |
| VocabFine | Fine-tuning | [480, 480, 224] | [0.75, 0.75, 1.5] | 75.6 | 70.5 | 73.8 | 35.3 | 65.0 | 61.5 | 65.9 | 34.9 |
| ClassFine | Fine-tuning | [480, 480, 224] | [0.75, 0.75, 1.5] | 75.6 | 68.9 | 72.4 | 33.9 | 64.3 | 60.7 | 64.9 | 34.9 |
| CT-CLIP | Zero-shot | [480, 480, 224] | [0.75, 0.75, 1.5] | 73.1 | 66.8 | 70.7 | 32.3 | 62.9 | 59.5 | 64.2 | 33.6 |
| BIUD | Zero-shot | [320, 224, 64] | – | 71.3 | 68.1 | 71.6 | 33.8 | 62.9 | 60.6 | 65.2 | 33.7 |
| Merlin | Zero-shot | [224, 224, 160] | [1.50, 1.50, 3.0] | 72.8 | 67.2 | 70.9 | 33.7 | 64.4 | 61.9 | 66.3 | 34.8 |
| fLVM | Zero-shot | [480, 352, 224] | [0.75, 0.75, 1.5] | 77.8 | 71.8 | 75.1 | 37.9 | 68.0 | 64.7 | 68.8 | 37.4 |
| BrgSA | Zero-shot | [224, 224, 112] | [1.50, 1.50, 3.0] | 79.2 | 73.3 | 76.2 | 38.5 | 70.0 | 65.5 | 69.3 | 39.1 |

Medical material: [catheter_or_port, tracheal_tube, chest_tube, breast_implant, pacemaker_or_defib, stent, clip, staple, gi_tube, hardware, suture],
Arterial wall calcification: [calcification],
Cardiomegaly: [cardiomegaly],
Pericardial effusion: [pericardial_effusion],
Coronary artery wall calcification: [calcification],
Hiatal hernia: [hernia],
Lymphadenopathy: [lymphadenopathy],
Emphysema: [emphysema],
Atelectasis: [atelectasis],
Lung nodule: [nodule, nodulegr1cm],
Lung opacity: [opacity],
Pulmonary fibrotic sequela: [scarring],
Pleural effusion: [pleural_effusion],
Mosaic attenuation pattern: None,
Peribronchial thickening: [bronchial_wall_thickening],
Consolidation: [consolidation],
Bronchiectasis: [bronchiectasis],
Interlobular septal thickening: [septal_thickening]

Fig. 5. Mapping of 27 abnormalities from RAD-ChestCT to 18 abnormalities in CT-RATE. The abnormalities from CT-RATE are denoted in blue font, whereas the abnormalities from RAD-ChestCT are denoted in black font.

the semantic consistency between image and text features and strengthens their alignment for downstream tasks.

In our experiments, α , β , and γ are empirically set to 0.5, 1, and 1, respectively, based on preliminary trials to balance the contributions of different loss components. K is set to 2048, as determined through the experimental search results presented later. We use the Adam optimizer with a learning rate of 5×10^{-5} . The batch size is set to 8 for all experiments. The code is implemented using the PyTorch framework, and all experiments are conducted on a single NVIDIA A800 GPU. During the inference phase, we set the prompt template as “There is [abnormality]” for zero-shot abnormality diagnosis.

4.4. Evaluation Metrics

For the multi-label classification, we adapt Area under the ROC Curve (AUC), Accuracy (ACC), F1 score, and Precision as metrics for evaluating zero-shot abnormality diagnosis. For volume-to-volume retrieval task, we use Mean Average Precision at Q (MAP@ Q) metrics, where Q represents the number of top-ranked retrieved volumes considered. In our experiment, Q is set to {5, 10, 50}. For the report-to-volume retrieval task, we use Recall@ P , where P represents the number of retrieved images, to measure the proportion of correctly matched images within the top- P retrieved results for a given query text. In our experiment, P is set to {5, 10, 50, 100}.

Table 2. Performance comparison for volume-to-volume retrieval task on CT-RATE-LT and RAD-ChestCT-LT datasets.

| Dataset | Method | AUC | ACC | F1 score | Precision |
|----------------|-----------|-------------|-------------|-------------|-------------|
| CT-RATE-LT | VocabFine | 69.2 | 71.2 | 79.5 | 2.2 |
| | CT-CLIP | 76.9 | 78.1 | 86.6 | 1.0 |
| | Merlin | 75.3 | 80.8 | 86.4 | 2.8 |
| | BrgSA | 85.6 | 88.5 | 93.3 | 4.3 |
| RAD-ChestCT-LT | VocabFine | 59.0 | 57.5 | 66.6 | 13.4 |
| | CT-CLIP | 58.2 | 56.9 | 66.2 | 13.1 |
| | Merlin | 59.1 | 57.0 | 66.1 | 13.6 |
| | BrgSA | 62.9 | 59.9 | 68.4 | 14.6 |

4.5. Comparison with State-of-the-art Methods

We compare our method against four zero-shot approaches, supervised learning, and fine-tuning methods, as summarized in Table 1. The evaluation is conducted on both internal (CT-RATE) and external (RAD-ChestCT) validation benchmarks for zero-shot abnormality diagnosis. In addition, we examine the input image shape and spacing used by each method. Note that when images are resized to a fixed shape without maintaining consistent resolution, the spacing becomes undefined. To provide a comprehensive evaluation, we detail the comparison methods as follows:

Supervised Learning Method:

- CT-Net (Draeos et al., 2021): This method uses a deep convolutional neural network with transfer learning and 3D convolutions to perform multi-disease classification.

Fine-tuning Methods:

- VocabFine (Hamamci et al., 2024): This method fine-tunes only the projection layers of the image and text encoders in CT-CLIP while freezing all other pre-trained layers, preserving open-vocabulary capabilities.
- ClassFine (Hamamci et al., 2024): This method adds and trains a new classification layer on CT-CLIP while optionally freezing the pre-trained layers to retain existing feature representations.

Zero-shot Methods:

- CT-CLIP (Hamamci et al., 2024): This method employs a contrastive vision-language pretraining approach to align 3D chest CT volumes with radiology reports, utilizing a vision transformer for 3D CT and a text transformer for embedding generation.
- BIUD (Cao et al., 2024): This method aligns 3D CT images with 2D X-ray images through a language-guided retrieval strategy and enhances alignment using robust contrastive learning and entity-focused masking.
- Merlin (Blankemeier et al., 2024): This method employs multi-task learning to process 3D abdominal CT volumes, by integrating structured electronic health record data and unstructured radiology reports, optimizing binary cross-entropy and InfoNCE losses to achieve effective vision-language alignment.
- fVLM (Anonymous, 2024): This method utilizes fine-grained contrastive learning for anatomy-level alignment between CT images and radiology reports. It addresses false negatives with a dual reduction strategy and employs co-teaching to improve semantic representation and diagnostic accuracy.

As shown in Table 1, our method achieves the highest evaluation metrics among all tested methods on both the CT-RATE and RAD-ChestCT datasets. Compared to supervised learning and fine-tuning methods, our approach demonstrates clear advantages, attributed to the proposed BrgSA framework for vision-language semantic alignment. While fVLM introduces fine-grained anatomy-level alignment to improve vision-language tasks, it overlooks the modality gap inherent in the CLIP embedding space, which limits its ability to fully align image and text features. In contrast, our BrgSA framework effectively narrows this gap by combining the semantic summarization module, which simplifies textual learning and extracts high-level semantic information, with the CMKI module, which optimizes image-text features by reducing their discrepancies and preserving their unique characteristics. This comprehensive approach ensures superior vision-language alignment and enables our method to achieve SOTA performance in zero-shot abnormality diagnosis. Surprisingly, our method achieves

Table 3. Performance comparison for volume-to-volume retrieval task on CT-RATE and RAD-ChestCT datasets.

| Dataset | Method | MAP@5 | MAP@10 | MAP@50 |
|-------------|-----------|-------------|-------------|-------------|
| CT-RATE | CT-Net | 59.4 | 48.1 | 40.7 |
| | VocabFine | 68.3 | 57.2 | 48.8 |
| | ClassFine | 67.9 | 56.8 | 48.5 |
| | CT-CLIP | 68.3 | 57.2 | 48.9 |
| | Merlin | 62.6 | 51.3 | 43.9 |
| | BrgSA | 69.2 | 58.5 | 50.5 |
| RAD-ChestCT | CT-Net | 71.2 | 58.9 | 52.4 |
| | VocabFine | 73.8 | 63.1 | 56.4 |
| | ClassFine | 73.8 | 63.1 | 56.3 |
| | CT-CLIP | 72.3 | 60.9 | 53.8 |
| | Merlin | 74.0 | 63.3 | 56.6 |
| | BrgSA | 74.3 | 63.8 | 57.2 |

Table 4. Performance comparison for report-to-volume retrieval task on CT-RATE dataset.

| Method | Recall@5 | Recall@10 | Recall@50 | Recall@100 |
|-----------|------------|-------------|-------------|-------------|
| VocabFine | 0.1 | 0.6 | 2.3 | 2.0 |
| CT-CLIP | 2.9 | 5.0 | 18.0 | 28.7 |
| Merlin | 1.5 | 2.7 | 7.7 | 12.7 |
| BrgSA | 5.8 | 10.1 | 28.6 | 42.0 |

outstanding performance using low-resolution 3D images, further highlighting its robustness and practicality for resource-constrained clinical environments.

To comprehensively evaluate the zero-shot diagnostic performance of our proposed method across various abnormalities, we introduce two new validation datasets in addition to existing public benchmarks (Hamamci et al., 2024): CT-RATE-LT, consisting of 15 types of abnormalities, and RAD-ChestCT-LT, which encompasses 56 previously untested categories from the RAD-ChestCT dataset. As shown in Table 2, we perform a comparative analysis of the performance of the open-source models and our proposed method on these two datasets. The results reveal that our method consistently outperforms other approaches in zero-shot diagnostic performance across a wide range of abnormalities. These improvements can be attributed to the effective vision-language alignment achieved by combining semantic summarization and CMKI module.

4.6. Volume-to-Volume Retrieval Task

In the volume-to-volume retrieval task, cosine similarity is used to rank reference volumes by their proximity to a query volume in a shared latent space. The latent embeddings are generated by a vision encoder trained with a contrastive learning framework to align semantic features across volumes. Relevance between the query and retrieved volumes is measured based on the overlap of their abnormality labels. The experiments are conducted on both the internal and external validation to ensure robustness under different distributions.

As shown in Table 3, our method achieves superior performance, which can be attributed to the cross-modal interaction

Table 5. Ablation study on the Semantic Summarization (SS) and the CMKI module for zero-shot abnormality diagnosis on the RAD-ChestCT dataset.

| SS | CMKI | AUC | ACC | F1 score | Precision |
|----|------|-------------|-------------|-------------|-------------|
| | | 65.0 | 61.1 | 65.4 | 35.7 |
| ✓ | | 67.9 | 64.0 | 67.9 | 37.2 |
| | ✓ | 68.0 | 64.0 | 67.9 | 38.0 |
| ✓ | ✓ | 70.0 | 65.5 | 69.3 | 39.1 |

module proposed in this study. By constructing the CMKB as a bridge for image-text features, our method effectively projects features into a shared space, significantly reducing the discrepancies between the image and text modalities. Furthermore, contrastive learning is employed to align the image and text features, allowing the model to capture highly discriminative semantic information from images. As a result, our method delivers outstanding performance in the volume-to-volume retrieval task.

4.7. Report-to-Volume Retrieval Task

The report-to-volume retrieval task matches textual descriptions in radiology reports with their corresponding 3D medical imaging volumes. Retrieval is performed by calculating cosine similarity between the text and image embeddings, ranking volumes based on similarity scores, and selecting the top- P most relevant ones. Since the RAD-ChestCT dataset does not include radiology reports, this evaluation is conducted on the CT-RATE dataset.

As shown in Table 4, VocabFine uses abnormality labels for fine-tuning. The training process retains some degree of vision-language alignment, but the images are only aligned with the labels and fail to achieve semantic alignment with the complete reports. This limitation results in the poorest performance in report-to-volume retrieval tasks. On the other hand, Merlin employs structured annotations to pre-train the vision encoder before aligning images and text. However, this strategy introduces bias into the image features, making effective semantic alignment difficult, which leads to poor retrieval results between images and reports. In contrast, our method leverages a large language model to semantically summarize the reports, combining the original reports and their semantic summaries during training. This approach reduces the textual training burden while preserving the rich semantic information in the reports. Our proposed BrgSA constructs a bridge between image and text information, enabling effective semantic alignment. Compared to CT-CLIP, our method achieves outstanding performance in the report-to-volume retrieval task, as evidenced by significant improvements in Recall@10 (5.0 vs. 10.1) and Recall@100 (28.7 vs. 42.0).

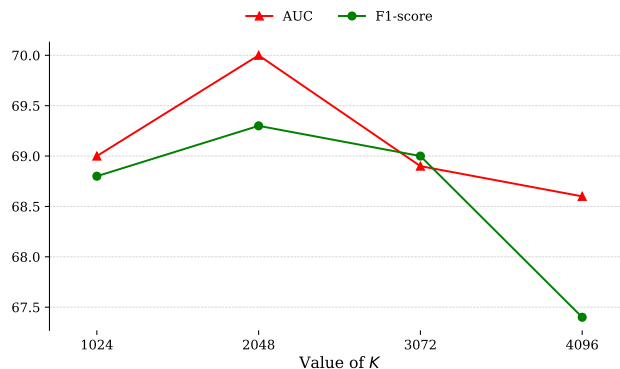
5. Discussion

5.1. Ablation Study

To evaluate the contributions of each module to the performance of BrgSA, we conduct ablation experiments on the zero-shot abnormality diagnosis and the report-to-volume retrieval

Table 6. Ablation study on the impact of the Semantic Summarization (SS) and the CMKI module for the report-to-volume retrieval task on the CT-RATE validation dataset.

| SS | CMKI | Recall@5 | Recall@10 | Recall@50 | Recall@100 |
|----|------|------------|-------------|-------------|-------------|
| | | 2.2 | 3.7 | 13.1 | 22.2 |
| ✓ | | 2.2 | 4.1 | 18.4 | 29.1 |
| | ✓ | 3.4 | 5.8 | 21.8 | 34.6 |
| ✓ | ✓ | 5.8 | 10.1 | 28.6 | 42.0 |

**Fig. 6. Results of varying K for CMKB on RAD-ChestCT dataset.**

tasks. The results are presented in Table 5 and Table 6, with CLIP used as the baseline. The proposed method incorporates two core modules: semantic summarization and CMKI.

First, the independent introduction of the semantic summarization module leads to a significant performance boost (AUC improves from 65.0 to 67.9 in Table 5, and Recall@50 increases from 13.1 to 18.4 in Table 6). By leveraging an LLM to perform semantic summarization of the reports, this module effectively reduces the complexity of textual feature learning. Consequently, it improves image-text alignment quality, leading to improved zero-shot diagnostic and retrieval performance.

Second, the independent introduction of the CMKI module similarly results in a substantial performance enhancement compared to the baseline (AUC is improved to 68.0 from 65.0 in Table 5, and Recall@50 is improved to 21.8 from 13.1 in Table 6). Specifically, in the report-to-volume retrieval task, the results demonstrate notable improvements, which can be attributed to the introduction of the CMKB as a bridge between image and text features. The CMKI module facilitates implicit alignment for unpaired image-text features by leveraging the shared latent space constructed by the CMKB. This process enables cross-modal information interaction, reduces discrepancies between modalities, and preserves the unique characteristics of each modality, thereby improving the alignment of image-text features and enhancing retrieval performance. In the zero-shot diagnostic task, the CMKI module effectively reduces the modality gap in vision-language alignment, enabling precise abnormality classification and demonstrating its capability to enhance cross-modal alignment for robust diagnostic inference.

Finally, by combining the semantic summarization and CMKI modules, BrgSA achieves the best performance (AUC:

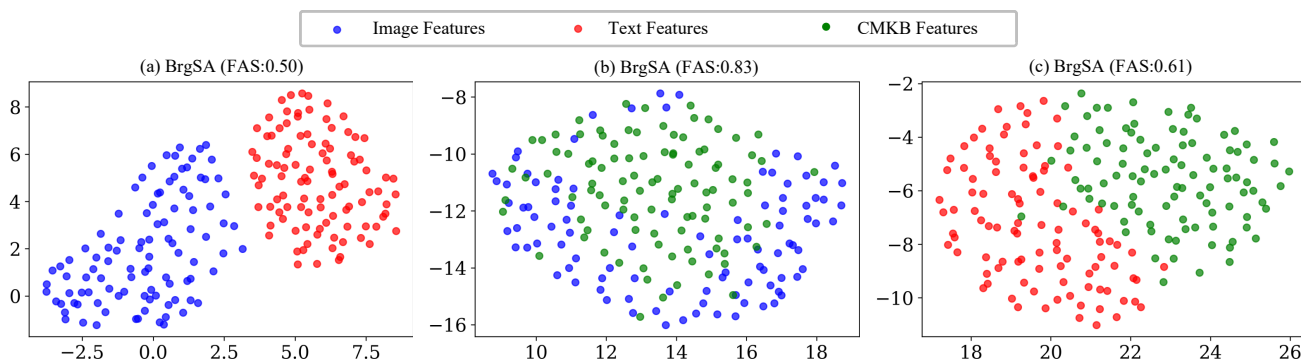


Fig. 7. UMAP visualization of features. Cosine similarity is used to evaluate the alignment between image and text features. The text features are generated using generic descriptive texts to ensure that all images can be matched to all texts. (a)–(c) represent features trained by BrgSA.

70.0 in Table 5, Recall@50: 28.6 in Table 6). The semantic summarization module simplifies textual learning and extracts high-level semantic information, while the CMKI module bridges the modality gap through implicit alignment and cross-modal interaction. Together, these modules enhance vision-language alignment, leading to improved performance in both zero-shot diagnosis and report-to-volume retrieval tasks.

5.2. Hyper-parameter of CMKB

The hyper-parameter K in CMKB, which defines the number of basis vectors, plays a pivotal role in determining its spatial representational capacity. To evaluate the influence of K , we conduct experiments with values $K = \{1024, 2048, 3072, 4096\}$. As illustrated in Fig. 6, increasing K enhances the spatial coverage of features and improve image-text alignment quality. However, this improvement diminishes and eventually saturates as K becomes excessively large. In such scenarios, an overabundance of basis vectors can hinder cross-modal information interaction. For instance, when K is excessively large, the model may reconstruct features independently within each modality, effectively bypassing the role of CMKI and nullifying cross-modal interaction. Based on these observations, we set $K = 2048$ for all subsequent experiments, as it strikes an optimal balance between alignment performance and computational efficiency.

5.3. Visualization of Features

Fig. 1 and Fig. 7 illustrate the UMAP visualization of image, text, and CMKB features. To assess the effectiveness of vision-language alignment, we ensure that all text descriptions are aligned with all CT volumes. As shown in Fig. 8, we leverage GPT-4 to generate multiple unbiased, generic descriptions of chest CT volumes as text samples for feature extraction. During the UMAP computation, cosine similarity is employed to measure the distances between different features, representing the degree of alignment among them. To quantify the impact of introducing CMKI on vision-language alignment, we define the Feature Alignment Score (FAS) as:

$$\text{FAS} = 1 - \text{Silhouette Score}, \quad (12)$$

where the silhouette score, originally used to evaluate cluster separation (Rousseeuw, 1987; Shahapure and Nicholas, 2020;

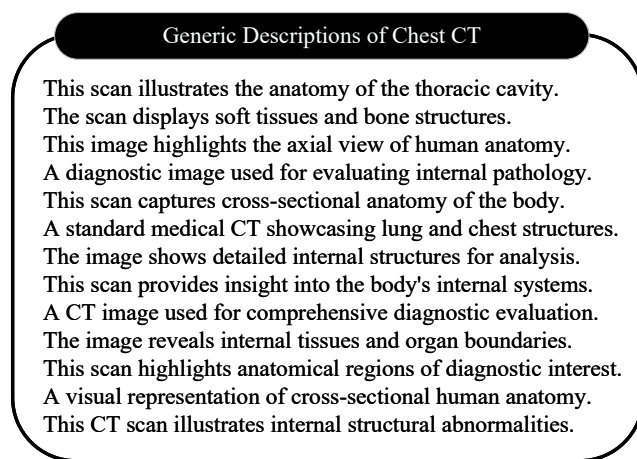


Fig. 8. Generic descriptions of chest CT generated by a LLM for visualizing text features.

Shutaywi and Kachouie, 2021), measures the cohesion of image and text feature sets. By normalizing the silhouette score to the range of $[0, 1]$, the FAS quantifies the alignment: a score closer to 1 indicates better alignment, while a score closer to 0 indicates poorer alignment.

Comparing Fig. 1 (b) and Fig. 7 (a), we observe that our proposed BrgSA framework significantly reduces the gap between image and text feature spaces, resulting in higher FAS values (0.37 vs. 0.50). This demonstrates that CMKI effectively enhances vision-language alignment. Further, Fig. 7 (b) and Fig. 7 (c) reveal that CMKB features align more closely with image features than with text features. This discrepancy can be attributed to the high-level abstraction and relatively uniform nature of text features, whereas image features are richer and more diverse. The greater variability in image feature representation makes CMKB features gravitate toward image features. Finally, as shown in Fig. 1 (c), CMKB features act as a bridge between image and text features, connecting the two feature spaces and facilitating their interaction. This bridging role effectively improves the overall vision-language alignment, further validating the importance of CMKB in this process.

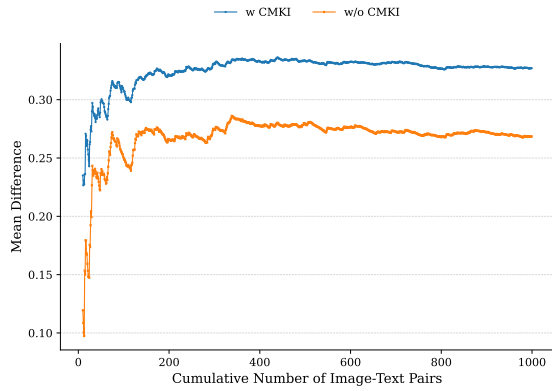


Fig. 9. Comparison of mean differences between paired and unpaired image-text samples on CT-RATE validation dataset.

5.4. Mean Difference for Pair-unpair Discrimination

The goal of CLIP is to increase the similarity of paired image-text samples while decreasing the similarity of unpaired image-text samples. To evaluate the quality of image-text alignment, we define the mean difference as follows:

$$\Delta_{\text{mean}} = \frac{1}{n(n-1)} \sum_{i=1}^n \sum_{j \neq i} (M(i, i) - M(i, j)), \quad (13)$$

where $M(i, i)$ represents the similarity of the i -th paired image-text sample, $M(i, j)$ represents the similarity between the i -th image and the j -th text, and n is the total number of image-text pairs. The results are evaluated on the CT-RATE validation set to demonstrate the effectiveness of the alignment.

Fig. 9 shows the variation of mean difference between paired and unpaired image-text samples. The horizontal axis represents the cumulative number of image-text pairs, and the vertical axis represents mean difference, Δ_{mean} . It can be observed that the methods incorporating the CMKI module achieve a higher Δ_{mean} curve compared to those without the CMKI module. This indicates that the CMKI module leads to a greater similarity difference between paired and unpaired samples, enabling better discrimination between them. This improvement is attributed to the role of CMKB as a bridge between image and text features. By projecting features from both modalities into a shared latent space, the CMKB effectively reduces the discrepancy between modalities while preserving their unique characteristics. This enhances the vision-language alignment and improves the ability to differentiate paired and unpaired image-text samples.

5.5. Limitations and future work

Despite the promising results achieved by our proposed method, several limitations remain to be addressed. First, while our method incorporates semantic summarization and cross-modal knowledge interaction for global feature alignment, it may still overlook fine-grained local details in 3D images, which are critical for certain complex abnormalities. Second, while the zero-shot setting demonstrates strong performance, further exploration of few-shot scenarios may provide more

comprehensive insights into the method’s adaptability and robustness.

In future work, we aim to address these limitations by enhancing the integration of fine-grained local feature alignment into our framework to better capture subtle details in 3D images. Additionally, extending the current approach to include few-shot learning settings and exploring its application in broader clinical scenarios will be the focus of our ongoing research.

6. Conclusion

This paper proposes a BrgSA framework to narrow the modality gap in 3D medical image-text alignment for zero-shot abnormality diagnosis. The BrgSA framework consists of a semantic summarization module and a CMKI module. The semantic summarization module leverages a large language model to summarize radiology reports, reducing the complexity of textual feature learning and generating high-level semantic representations. The CMKI module facilitates cross-modal interaction between image and text features, effectively reducing modality discrepancies while preserving their unique characteristics. Leveraging these components, the BrgSA framework effectively reduces the modality gap and achieves robust vision-language alignment. Experimental results validate its efficacy, demonstrating competitive performance in both zero-shot diagnosis and retrieval tasks across internal and external validation datasets.

Data availability

The code and model will be made publicly available online. The dataset used is publicly accessible online. Additionally, the custom annotations will also be made available online.

Declaration of Generative AI and AI-assisted technologies in the writing process

During the preparation of this work the author(s) used GPT-4 from OpenAI in order to improve readability and language. After using this tool/service, the author(s) reviewed and edited the content as needed and take(s) full responsibility for the content of the publication.

Acknowledgments

This work was supported by Natural Science Foundation of China under Grant 62271465, Suzhou Basic Research Program under Grant SYG202338, and Open Fund Project of Guangdong Academy of Medical Sciences, China (No. YKY-KF202206).

Supplementary material

Supplementary material is prepared and provided as a separate file along with the manuscript.

References

- Achiam, J., Adler, S., Agarwal, S., Ahmad, L., Akkaya, I., Aleman, F.L., Almeida, D., Altenschmidt, J., Altman, S., Anadkat, S., et al., 2023. Gpt-4 technical report. arXiv preprint arXiv:2303.08774 .
- Anonymous, 2024. Large-scale and fine-grained vision-language pre-training for enhanced CT image understanding, in: Submitted to The Thirteenth International Conference on Learning Representations. URL: <https://openreview.net/forum?id=nYpPAT4L3D>. under review.
- Bera, K., Schalper, K.A., Rimm, D.L., Velcheti, V., Madabhushi, A., 2019. Artificial intelligence in digital pathology—new tools for diagnosis and precision oncology. *Nature reviews Clinical oncology* 16, 703–715.
- Blankemeier, L., Cohen, J.P., Kumar, A., Van Veen, D., Gardezi, S.J.S., Paschali, M., Chen, Z., Delbrouck, J.B., Reis, E., Truys, C., et al., 2024. Merlin: A vision language foundation model for 3d computed tomography. *Research Square*, rs-3.
- Bustos, A., Pertusa, A., Salinas, J.M., De La Iglesia-Vaya, M., 2020. Padchest: A large chest x-ray image dataset with multi-label annotated reports. *Medical image analysis* 66, 101797.
- Cao, W., Zhang, J., Xia, Y., Mok, T.C., Li, Z., Ye, X., Lu, L., Zheng, J., Tang, Y., Zhang, L., 2024. Bootstrapping chest ct image understanding by distilling knowledge from x-ray expert models, in: Proceedings of the IEEE/CVF Conference on Computer Vision and Pattern Recognition, pp. 11238–11247.
- Chen, Z., Du, Y., Hu, J., Liu, Y., Li, G., Wan, X., Chang, T.H., 2022. Multi-modal masked autoencoders for medical vision-and-language pre-training, in: International Conference on Medical Image Computing and Computer-Assisted Intervention, Springer.
- Deng, C., Tang, X., Yan, J., Liu, W., Gao, X., 2015. Discriminative dictionary learning with common label alignment for cross-modal retrieval. *IEEE Transactions on Multimedia* 18, 208–218.
- Dosovitskiy, A., Beyer, L., Kolesnikov, A., Weissenborn, D., Zhai, X., Unterthiner, T., Dehghani, M., Minderer, M., Heigold, G., Gelly, S., et al., 2020. An image is worth 16x16 words: Transformers for image recognition at scale. arXiv preprint arXiv:2010.11929 .
- Draeos, R.L., Dov, D., Mazurowski, M.A., Lo, J.Y., Henao, R., Rubin, G.D., Carin, L., 2021. Machine-learning-based multiple abnormality prediction with large-scale chest computed tomography volumes. *Medical image analysis* 67, 101857.
- Eslami, S., de Melo, G., 2024. Mitigate the gap: Investigating approaches for improving cross-modal alignment in clip. arXiv preprint arXiv:2406.17639 .
- Geuenich, M.J., Gong, D.w., Campbell, K.R., 2024. The impacts of active and self-supervised learning on efficient annotation of single-cell expression data. *Nature Communications* 15, 1014.
- Ginat, D.T., Gupta, R., 2014. Advances in computed tomography imaging technology. *Annual review of biomedical engineering* 16, 431–453.
- Gu, Y., Tinn, R., Cheng, H., Lucas, M., Usuyama, N., Liu, X., Naumann, T., Gao, J., Poon, H., 2021. Domain-specific language model pretraining for biomedical natural language processing. *ACM Transactions on Computing for Healthcare (HEALTH)* 3, 1–23.
- Hamamci, I.E., Er, S., Almas, F., Simsek, A.G., Esirgun, S.N., Dogan, I., Dasdelen, M.F., Wittmann, B., Simsar, E., Simsar, M., et al., 2024. A foundation model utilizing chest ct volumes and radiology reports for supervised-level zero-shot detection of abnormalities. arXiv preprint arXiv:2403.17834 .
- He, K., Zhao, W., Xie, X., Ji, W., Liu, M., Tang, Z., Shi, Y., Shi, F., Gao, Y., Liu, J., et al., 2021. Synergistic learning of lung lobe segmentation and hierarchical multi-instance classification for automated severity assessment of covid-19 in ct images. *Pattern recognition* 113, 107828.
- Huang, S.C., Pareek, A., Jensen, M., Lungren, M.P., Yeung, S., Chaudhari, A.S., 2023. Self-supervised learning for medical image classification: a systematic review and implementation guidelines. *NPJ Digital Medicine* 6, 74.
- Huang, S.C., Shen, L., Lungren, M.P., Yeung, S., 2021a. Gloria: A multimodal global-local representation learning framework for label-efficient medical image recognition, in: Proceedings of the IEEE/CVF International Conference on Computer Vision, pp. 3942–3951.
- Huang, Z., Zeng, Z., Huang, Y., Liu, B., Fu, D., Fu, J., 2021b. Seeing out of the box: End-to-end pre-training for vision-language representation learning, in: Proceedings of the IEEE/CVF conference on computer vision and pattern recognition, pp. 12976–12985.
- Johnson, A.E., Pollard, T.J., Berkowitz, S.J., Greenbaum, N.R., Lungren, M.P., Deng, C.y., Mark, R.G., Horng, S., 2019. MIMIC-CXR, a de-identified publicly available database of chest radiographs with free-text reports. *Scientific data* 6, 317.
- Kim, W., Son, B., Kim, I., 2021. Vilt: Vision-and-language transformer without convolution or region supervision, in: International conference on machine learning, PMLR. pp. 5583–5594.
- Lai, H., Yao, Q., Jiang, Z., Wang, R., He, Z., Tao, X., Zhou, S.K., 2024. Carzero: Cross-attention alignment for radiology zero-shot classification, in: Proceedings of the IEEE/CVF Conference on Computer Vision and Pattern Recognition, pp. 11137–11146.
- Li, S., Wang, L., Wang, S., Kong, D., Yin, B., 2023a. Hierarchical coupled discriminative dictionary learning for zero-shot learning. *IEEE Transactions on Circuits and Systems for Video Technology* 33, 4973–4984.
- Li, W., Gao, C., Niu, G., Xiao, X., Liu, H., Liu, J., Wu, H., Wang, H., 2022. Unimo-2: End-to-end unified vision-language grounded learning. arXiv preprint arXiv:2203.09067 .
- Li, Y., Shen, Y., Zhang, J., Song, S., Li, Z., Ke, J., Shen, D., 2023b. A hierarchical graph v-net with semi-supervised pre-training for histological image based breast cancer classification. *IEEE Transactions on Medical Imaging* .
- Liang, V.W., Zhang, Y., Kwon, Y., Yeung, S., Zou, J.Y., 2022. Mind the gap: Understanding the modality gap in multi-modal contrastive representation learning. *Advances in Neural Information Processing Systems* 35, 17612–17625.
- Lin, J., Xia, Y., Zhang, J., Yan, K., Lu, L., Luo, J., Zhang, L., 2024. Ct-glip: 3d grounded language-image pretraining with ct scans and radiology reports for full-body scenarios. arXiv preprint arXiv:2404.15272 .
- Long, Y., Liu, L., Shao, L., Shen, F., Ding, G., Han, J., 2017. From zero-shot learning to conventional supervised classification: Unseen visual data synthesis, in: Proceedings of the IEEE conference on computer vision and pattern recognition, pp. 1627–1636.
- Lu, J., Batra, D., Parikh, D., Lee, S., 2019. Vilbert: Pretraining task-agnostic visiolinguistic representations for vision-and-language tasks. *Advances in neural information processing systems* 32.
- Mei, L., Deng, K., Cui, Z., Fang, Y., Li, Y., Lai, H., Tonetti, M.S., Shen, D., 2025. Clinical knowledge-guided hybrid classification network for automatic periodontal disease diagnosis in x-ray image. *Medical Image Analysis* 99, 103376.
- Oikonomou, E.K., Marwan, M., Desai, M.Y., Mancio, J., Alashi, A., Centeno, E.H., Thomas, S., Herdman, L., Kotanidis, C.P., Thomas, K.E., et al., 2018. Non-invasive detection of coronary inflammation using computed tomography and prediction of residual cardiovascular risk (the crisp ct study): a post-hoc analysis of prospective outcome data. *The Lancet* 392, 929–939.
- Pellegrini, C., Keicher, M., Özsoy, E., Jiraskova, P., Braren, R., Navab, N., 2023. Xplainer: From x-ray observations to explainable zero-shot diagnosis, in: International Conference on Medical Image Computing and Computer-Assisted Intervention, Springer. pp. 420–429.
- Qian, X., Pei, J., Han, C., Liang, Z., Zhang, G., Chen, N., Zheng, W., Meng, F., Yu, D., Chen, Y., et al., 2024. A multimodal machine learning model for the stratification of breast cancer risk. *Nature Biomedical Engineering* , 1–15.
- Radford, A., Kim, J.W., Hallacy, C., Ramesh, A., Goh, G., Agarwal, S., Sastry, G., Askell, A., Mishkin, P., Clark, J., et al., 2021. Learning transferable visual models from natural language supervision, in: International conference on machine learning, PMLR. pp. 8748–8763.
- Rousseeuw, P.J., 1987. Silhouettes: a graphical aid to the interpretation and validation of cluster analysis. *Journal of computational and applied mathematics* 20, 53–65.
- Schrodi, S., Hoffmann, D.T., Argus, M., Fischer, V., Brox, T., 2024. Two effects, one trigger: On the modality gap, object bias, and information imbalance in contrastive vision-language representation learning. arXiv preprint arXiv:2404.07983 .
- Shahapure, K.R., Nicholas, C., 2020. Cluster quality analysis using silhouette score, in: 2020 IEEE 7th international conference on data science and advanced analytics (DSAA), IEEE. pp. 747–748.
- Shutaywi, M., Kachouie, N.N., 2021. Silhouette analysis for performance evaluation in machine learning with applications to clustering. *Entropy* 23, 759.
- Svoboda, E., 2020. Artificial intelligence is improving the detection of lung cancer. *Nature* 587, S20–S20.
- Taherdoost, H., 2024. Beyond supervised: The rise of self-supervised learning in autonomous systems. *Information* 15, 491.
- Tiu, E., Talus, E., Patel, P., Langlotz, C.P., Ng, A.Y., Rajpurkar, P., 2022. Expert-level detection of pathologies from unannotated chest x-ray images via self-supervised learning. *Nature Biomedical Engineering* 6, 1399–1406.
- Tyshchuk, K., Karpikova, P., Spiridonov, A., Prutianova, A., Razzhigaev, A.,

- Panchenko, A., 2023. On isotropy of multimodal embeddings. *Information* 14, 392.
- Wang, C., Shao, J., He, Y., Wu, J., Liu, X., Yang, L., Wei, Y., Zhou, X.S., Zhan, Y., Shi, F., et al., 2024. Data-driven risk stratification and precision management of pulmonary nodules detected on chest computed tomography. *Nature Medicine* , 1–12.
- Wang, F., Zhou, Y., Wang, S., Vardhanabhuti, V., Yu, L., 2022a. Multi-granularity cross-modal alignment for generalized medical visual representation learning. *Advances in Neural Information Processing Systems* 35, 33536–33549.
- Wang, J., Zhang, F., Jia, X., Wang, X., Zhang, H., Ying, S., Wang, Q., Shi, J., Shen, D., 2022b. Multi-class asd classification via label distribution learning with class-shared and class-specific decomposition. *Medical Image Analysis* 75, 102294.
- Wang, Z., Wu, Z., Agarwal, D., Sun, J., 2022c. Medclip: Contrastive learning from unpaired medical images and text, in: *Proceedings of the 2022 Conference on Empirical Methods in Natural Language Processing*, pp. 3876–3887.
- Wu, C., Zhang, X., Zhang, Y., Wang, Y., Xie, W., 2023. Medklip: Medical knowledge enhanced language-image pre-training. *medRxiv* , 2023–01.
- Yao, L., Han, J., Wen, Y., Liang, X., Xu, D., Zhang, W., Li, Z., Xu, C., Xu, H., 2022. Detclip: Dictionary-enriched visual-concept paralleled pre-training for open-world detection. *Advances in Neural Information Processing Systems* 35, 9125–9138.
- Yoon, J.S., Oh, K., Shin, Y., Mazurowski, M.A., Suk, H.I., 2023. Domain generalization for medical image analysis: A survey. *arXiv preprint arXiv:2310.08598* .
- Yu, X., Zhang, L., Wu, Z., Zhu, D., 2024. Core-periphery multi-modality feature alignment for zero-shot medical image analysis. *IEEE Transactions on Medical Imaging* .
- Zhang, J., Wu, X., Tang, X., Zhou, L., Wang, L., Wu, W., Shen, D., 2024a. Asynchronous functional brain network construction with spatiotemporal transformer for mci classification. *IEEE Transactions on Medical Imaging* .
- Zhang, J., Zhou, L., Wang, L., Liu, M., Shen, D., 2022. Diffusion kernel attention network for brain disorder classification. *IEEE Transactions on Medical Imaging* 41, 2814–2827.
- Zhang, K., Yang, Y., Yu, J., Jiang, H., Fan, J., Huang, Q., Han, W., 2023a. Multi-task paired masking with alignment modeling for medical vision-language pre-training. *IEEE Transactions on Multimedia* .
- Zhang, X., Wu, C., Zhang, Y., Xie, W., Wang, Y., 2023b. Knowledge-enhanced visual-language pre-training on chest radiology images. *Nature Communications* 14, 4542.
- Zhang, Z., Ke, W., Zhu, Y., Liang, X., Liu, J., Ye, Q., Zhang, T., 2024b. Language-driven visual consensus for zero-shot semantic segmentation. *IEEE Transactions on Circuits and Systems for Video Technology* .
- Zhao, Z., Liu, Y., Wu, H., Wang, M., Li, Y., Wang, S., Teng, L., Liu, D., Cui, Z., Wang, Q., et al., 2023. Clip in medical imaging: A comprehensive survey. *arXiv preprint arXiv:2312.07353* .

Supplementary Material

As shown in Table S1–S4, we provide a comprehensive benchmark of different methods on the CT-RATE-LT dataset. Specifically, we present the detailed performance metrics for each abnormality, including Area under the ROC Curve (AUC), Accuracy, F1 score and Precision. These results enable a direct comparison of the effectiveness of various methods in detecting specific abnormalities, offering valuable insights into their strengths and limitations.

Table S1. AUC comparison of different methods for various abnormalities on CT-RATE-LT. The best performance is highlighted as bold.

| Method | PN | ATH | SPD | PTX | BT | OST | EMP | LC | LM | PC | PMD | PF | TB | PLC | RF | Mean |
|-----------|--------------|--------------|--------------|--------------|--------------|--------------|--------------|--------------|--------------|--------------|--------------|--------------|--------------|--------------|--------------|--------------|
| VocabFine | 66.73 | 80.94 | 60.45 | 61.80 | 36.40 | 99.36 | 96.48 | 54.08 | 67.76 | 97.14 | 74.99 | 6.32 | 67.34 | 85.25 | 82.69 | 69.18 |
| CT-CLIP | 63.99 | 78.46 | 65.32 | 74.15 | 63.78 | 76.70 | 93.25 | 64.19 | 84.41 | 77.66 | 90.29 | 94.11 | 91.16 | 81.93 | 54.51 | 76.93 |
| Merlin | 59.85 | 84.04 | 59.40 | 84.54 | 68.42 | 59.28 | 95.34 | 77.54 | 67.06 | 79.34 | 31.89 | 84.71 | 90.32 | 92.76 | 95.56 | 75.34 |
| BrgSA | 79.51 | 87.05 | 84.16 | 98.50 | 65.75 | 97.54 | 97.28 | 83.26 | 84.15 | 79.01 | 74.93 | 73.71 | 95.46 | 84.43 | 99.51 | 85.62 |

Note: PN: Pneumonia, ATH: Atherosclerosis, SPD: Spondylosis, PTX: Pneumothorax, BT: Bronchial thickening, OST: Osteophyte, EMP: Empyema, LC: Lung cyst, LM: Lung mass, PC: Pericardial calcification, PMD: Pneumomediastinum, PF: Pulmonary fibrosis, TB: Tuberculosis, PLC: Pleural calcification, RF: Rib fracture.

Table S2. Accuracy comparison of different methods for various abnormalities on CT-RATE-LT.

| Method | PN | ATH | SPD | PTX | BT | OST | EMP | LC | LM | PC | PMD | PF | TB | PLC | RF | Mean |
|-----------|--------------|--------------|--------------|--------------|--------------|--------------|--------------|--------------|--------------|--------------|--------------|--------------|--------------|--------------|--------------|--------------|
| VocabFine | 85.46 | 98.65 | 87.33 | 46.36 | 44.72 | 99.70 | 95.82 | 47.58 | 62.32 | 96.38 | 71.67 | 5.82 | 58.54 | 84.76 | 82.43 | 71.17 |
| CT-CLIP | 86.97 | 93.85 | 67.62 | 81.34 | 45.87 | 80.85 | 91.25 | 59.20 | 79.99 | 76.21 | 86.57 | 92.79 | 93.78 | 81.80 | 53.97 | 78.14 |
| Merlin | 81.90 | 99.34 | 49.29 | 99.64 | 96.05 | 44.52 | 93.45 | 91.94 | 89.93 | 88.32 | 12.90 | 82.23 | 95.33 | 92.66 | 95.06 | 80.84 |
| BrgSA | 89.60 | 98.88 | 97.43 | 98.91 | 83.84 | 99.47 | 96.78 | 80.29 | 83.19 | 76.54 | 74.10 | 70.25 | 94.37 | 84.37 | 99.47 | 88.50 |

Table S3. F1 score comparison of different methods for various abnormalities on CT-RATE-LT.

| Method | PN | ATH | SPD | PTX | BT | OST | EMP | LC | LM | PC | PMD | PF | TB | PLC | RF | Mean |
|-----------|--------------|--------------|--------------|--------------|--------------|--------------|--------------|--------------|--------------|--------------|--------------|--------------|--------------|--------------|--------------|--------------|
| VocabFine | 89.08 | 98.87 | 92.99 | 63.13 | 61.65 | 99.77 | 97.80 | 64.41 | 76.72 | 98.09 | 83.43 | 10.89 | 73.78 | 91.72 | 90.33 | 79.51 |
| CT-CLIP | 89.90 | 96.36 | 80.43 | 89.53 | 62.71 | 89.32 | 95.36 | 74.30 | 88.82 | 86.43 | 92.74 | 96.20 | 96.73 | 89.96 | 70.06 | 86.59 |
| Merlin | 86.97 | 99.22 | 65.76 | 99.65 | 97.83 | 61.50 | 96.55 | 95.74 | 94.63 | 93.73 | 22.75 | 90.18 | 97.54 | 96.16 | 97.44 | 86.38 |
| BrgSA | 91.78 | 99.00 | 98.46 | 99.30 | 91.06 | 99.66 | 98.30 | 89.00 | 90.76 | 86.64 | 85.06 | 82.46 | 97.04 | 91.49 | 99.71 | 93.31 |

Table S4. Precision comparison of different methods for various abnormalities on CT-RATE-LT.

| Method | PN | ATH | SPD | PTX | BT | OST | EMP | LC | LM | PC | PMD | PF | TB | PLC | RF | Mean |
|-----------|--------------|--------------|-------------|--------------|-------------|--------------|-------------|-------------|-------------|-------------|-------------|-------------|-------------|-------------|-------------|-------------|
| VocabFine | 7.95 | 6.67 | 0.52 | 0.37 | 0.18 | 12.50 | 1.55 | 0.13 | 0.17 | 1.79 | 0.23 | 0.07 | 0.16 | 0.22 | 0.19 | 2.18 |
| CT-CLIP | 7.53 | 2.22 | 0.61 | 0.53 | 0.30 | 0.34 | 0.75 | 0.16 | 0.33 | 0.28 | 0.49 | 0.90 | 0.53 | 0.18 | 0.07 | 1.01 |
| Merlin | 6.92 | 14.29 | 0.45 | 14.29 | 0.85 | 0.18 | 1.00 | 0.41 | 0.33 | 0.28 | 0.08 | 0.37 | 0.70 | 0.45 | 0.66 | 2.75 |
| BrgSA | 16.56 | 8.70 | 5.13 | 11.43 | 0.41 | 11.76 | 2.00 | 0.33 | 0.39 | 0.28 | 0.25 | 0.22 | 1.16 | 0.21 | 5.88 | 4.31 |